Super-Resolution Photoelectron Imaging with Real-Time Subpixelation by Field Programmable Gate Array and Its Application to NO and Benzene Photoionization†

Yoshihiro Ogi, Hiroshi Kohguchi,*,‡ Dongmei Niu, Keijiro Ohshimo, and Toshinori Suzuki*,§

Chemical Dynamics Laboratory, RIKEN Advanced Science Institute, 2-1 Hirosawa, Wako 351-0198, Japan

Received: April 30, 2009; Revised Manuscript Received: September 12, 2009

We have constructed a photoelectron imaging spectrometer with super-resolution image processing and have applied it to the photoionization of nitric oxide and benzene in molecular beams. A field programmable gate array is employed for real-time subpixel centroiding calculations on hardware, providing 64 megapixel resolution (8192 × 8192 pixels). We examined eight different centroiding algorithms based on the center-of-gravity (COG) and Gaussian fitting (Gauss) methods and have found that the two-dimensional COG (2D-COG) and weighted mean of Gaussian center (w-Gauss) methods have the best performance. The excellent performance of the instrument is demonstrated by visualizing a 25 μm diameter pore structure of an MCP, indicating a spatial resolution of 0.03%. The photoelectron image in one-color (1 + 1) resonance-enhanced multiphoton ionization of nitric oxide using a nanosecond laser provided a photoelectron kinetic energy resolution of 0.2%. This resolution is currently restricted by charged-particle optics. The photoelectron energy and angular distributions in the one-color (1 + 1) resonance-enhanced multiphoton ionization of benzene via 6^1 and $6^1 1^1$ vibronic levels in the S_1 state are also presented. The results demonstrate that photoelectron angular anisotropy varies with the photoelectron kinetic energy and the vibronic state of the cation.

I. Introduction

The ultimate goal of scattering experiments in reaction dynamics study is the measurement of multiply differential cross sections. The measurement requires highly sensitive detection, because the expected signal intensity is extremely low. The demand for higher sensitivity has stimulated technological advances in position-sensitive detectors (PSDs) that register two-dimensional (2D) arrival positions of charged particles (electrons or ions). A 2D PSD allows highly efficient and accurate measurements of differential cross sections, since it can be used to observe scattering products at all solid angles simultaneously. On the other hand, the resolution and accuracy obtainable with 2D detectors have been thought to be inferior to those obtainable by conventional detection methods. In fact, a time-of-flight (TOF) apparatus with a flight tube of 1 m provides a higher resolution in velocity vector measurement than 2D detectors with diameters of 80 mm. Nonetheless, further improvement in the resolution will certainly make 2D PSDs ideal instruments because of their high efficiencies. With this consideration, various efforts have already been made.[1−4]

Obviously, the size of a charged particle incident on a PSD is far smaller than the resolution of the detector. Therefore, the key is the spatial response function of the device, i.e., how finely the position of a particle impact on a detector can be measured. In a photoionization study using pulsed lasers, the simultaneous detection of at least ten particles is required. Therefore, we employ a camera-based 2D PSD and not a delay line detector that can handle only several hits simultaneously. At the impact energies of several kiloelectronvolts considered in this paper, an incoming particle cannot efficiently excite a phosphor plate that visualizes the arrival position by a camera. Therefore, microchannel plates (MCPs) are employed to amplify the secondary electrons to excite the phosphor screen. The amplification factor is $\sim 10^6$. As a result, the ultimate position resolution of the 2D PSD is limited by the pore-to-pore interval of an MCP.

Signal processing is clearly needed to reach such a resolution. An MCP has millions of microchannels 5−25 μm in diameter. Since their gain factor is ~1000/plate, 2D detectors generally employ dual plates to achieve a gain factor of $\sim 10^6$. Even if a charged particle enters a single channel of the first MCP, excitation can leak to adjacent channels in the multistage MCP assembly, so that spatial resolution degrades. Furthermore, when amplified electrons are emitted from the MCPs to excite a phosphor screen, space charge blurs the electron beam. Thus, the light spot appearing on the phosphor screen spreads over an area of ~100 μm in diameter, and the super-resolution processing of centroiding and the binarization of the light spot is indispensable for recovering spatial resolution.

Centroiding processing in the particle imaging has long been developed in the field of astronomy and high-energy physics for single-photon imaging.[5−16] The algorithms and standards for defining a centroid have been investigated theoretically and numerically. One of the most serious problems in achieving super-resolution by centroiding calculations is the occurrence of a fixed pattern noise (FPN), an artificial noise with a particular spatial pattern: a typical FPN appears along the four boundaries of an N-by-N subpixel unit. It has been pointed out that an FPN mostly originates from the centroiding algorithm that is unsuitable for the shape of a blurred spot.[8]

Since a high-resolution camera can image a light spot more finely, it should allow more accurate centroiding. However, the larger the number of pixels of an image sensor ($N_{sensor} \times N_{sensor}$), the smaller the number of frames readable per second. Because

† Part of the "Vincenzo Aquilanti Festschrift".

* Corresponding authors, kohguchi@hiroshima-u.ac.jp and t-suzuki@riken.jp.

‡ Present address: Department of Chemistry, School of Science, Hiroshima University, Kagamiyama 1-3-1, Higashi-Hiroshima 739-8526, Japan.

§ Also at Department of Chemistry, Graduate School of Science, Kyoto University, Kyoto, 606-8502, Japan.

10.1021/jp9039995
Published on Web 10/09/2009

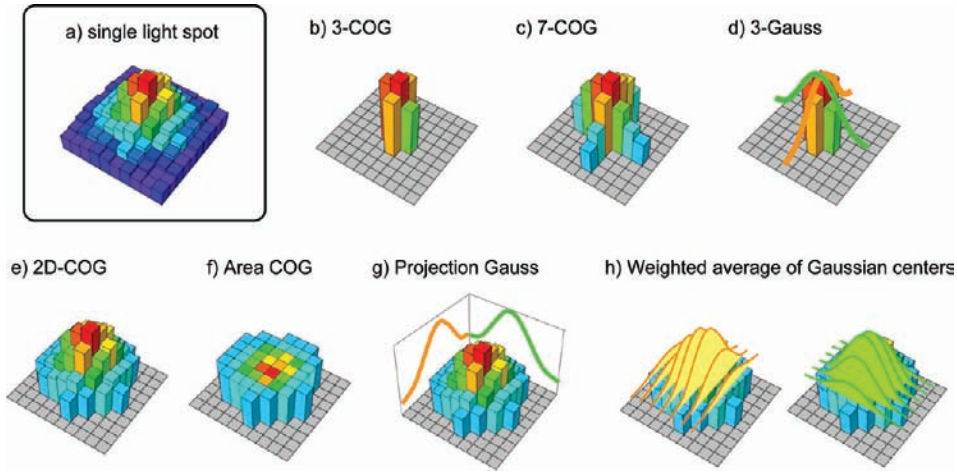

Figure 1. (a) Example of the intensity distribution of one light spot detected on the phosphor screen by a CCD camera. (b−h) Conceptual illustrations of the centroiding algorithms tested in this study to explain which pixels are adopted and how they are treated in the centroiding calculations: (b) 3-COG, (c) 7-COG, (d) 3-Gauss, (e) 2D-COG, (f) a-COG, (g) p-Gauss, and (h) w-Gauss algorithms (see text for explicit expressions).

the centroiding calculation requires no overlap of light spots in one frame, there is a minimum frame rate required for measurements, depending on signal count rate; consequently, there is also a maximum number of pixels allowed for each application. The dynamic range is another important characteristic of a camera for centroiding, because the intensity profile of a light spot is crucial for accurate centroiding. Currently, commercially available CCD (charge-coupled device) and CMOS (complementary metal oxide semiconductor) image sensors have $N_{sensor} = 256-2048$ and read-out rates of 10−1000 frames/s. Although CMOS sensors have a large number of pixels and high frame rates, their sensitivities are too low to be used for 2D detectors without an image intensifier. Because image intensifiers lower spatial resolution, a superior resolution is anticipated for a CCD. In imaging with megapixel CCD sensors, $^1/_2$ to $^1/_8$ of a pixel corresponds to the MCP pore interval. Therefore, if this level of subpixelation is achieved, we obtain the ultimate resolution limited only by the MCP pore interval.

Centroiding is executable by either off-line processing[1] after the measurement of all the image frames recorded as streaming data or online real-time processing[4,17,18] that completes the centroiding calculations of each image frame before the next image frame is transferred from a sensor. The advantage of off-line processing is its flexibility. In this work, we used off-line processing for comparing the performances of different centroiding algorithms prior to programming on hardware. On the other hand, online processing is necessary in practical applications for rapid measurements and the compression of data size. Online processing is usually performed using software on a computer; however, its speed is too low to handle large image data with high dynamic ranges at high frame rates. To solve this problem, real-time image processing using a field-programmable gate array (FPGA) is promising, as the calculations are executed not by CPU but by logic gate arrays that provide a much higher speed. For instance, recently, we have achieved the real-time processing of a 512 × 512 image at 1 kHz using a CMOS camera and an FPGA circuit.[4] FPGA maintains flexibility in operation, because the code for calculation is described by a hardware description language (HDL) similar to standard computer languages and is rewritable. The FPGA device is expected to provide a new paradigm of laboratory instruments, especially in the area of imaging.[4]

Note that another important benefit of centroiding and binarization is that they markedly improve the uniformity of 2D PSD. An MCP detector has inevitable sensitivity variation over the area; the effect of a channel bias angle is particularly problematic in electron detection.[4] Centroiding calculation allows particle-counting (electron-counting or ion-counting) detection, which corrects the stochastic variation in the light spot brightness on the phosphor screen and counts the number of arriving particles correctly.

In this paper, we present the development of a high-resolution imaging system equipped with a FPGA circuit for real-time centroiding calculation. The method is applied to the photoionization of nitric oxide and benzene.

II. Centroiding Algorithms

We consider various centroiding algorithms for calculating the centroid (x_c, y_c) of an observed light spot. Figure 1a schematically shows an example of the intensity distribution of a single light spot on the phosphor screen observed by a CCD camera. The height of each bar represents the signal intensity of a CCD pixel. Parts b−h of Figure 1 illustrate the pixels that are to be taken into account in each centroiding algorithm. There are two major approaches, i.e., the 1D and 2D methods. 1D algorithms (Figure 1b−d) first search for the center pixel (x_0, y_0) (pixel with the maximum value inside the spot) and then consider pixels located in the same row (i, y_0) or column (x_0, j). 2D algorithms (Figure 1e−h) consider all pixels having a value higher than the preset threshold. Note that the integer value is used as an original pixel position in the calculation.

In the centroiding calculation, there are two types of mathematical numerations: center-of-gravity (COG) calculation and Gaussian fitting (Gauss). *n*-Point center-of-gravity (*n*-COG) algorithms utilize the center pixel (x_0, y_0) and its wings. For instance, 3-COG ($n = 3$, Figure 1b) determines the centroid x_c from three pixels on the horizontal line (row) of the cross. The explicit formula is

$$x_c = x_0 + \frac{P_{x_0+1} - P_{x_0-1}}{P_{x_0-1} + P_{x_0} + P_{x_0+1}} \quad (1)$$

where P_i is the pixel value at $(x, y) = (i, y_0)$. Similarly, y_c is determined from three pixels on the vertical line (column) of the cross using

$$y_c = y_0 + \frac{P_{y_0+1} - P_{y_0-1}}{P_{y_0-1} + P_{y_0} + P_{y_0+1}} \quad (1')$$

where P_j is the pixel value at $(x, y) = (x_0, j)$. Accordingly, x_c and y_c are determined independently in all algorithms. Hereafter, only the formulas for x_c are given, as similar formulas for y_c can be easily derived. 7-COG ($n = 7$, Figure 1c) employs the center pixel and three pixels on each side.

$$x_c = x_0 + \frac{(P_{x_0+1} + 2P_{x_0+2} + 3P_{x_0+3}) - (P_{x_0-1} + 2P_{x_0-2} + 3P_{x_0-3})}{P_{x_0-3} + P_{x_0-2} + P_{x_0-1} + P_{x_0} + P_{x_0+1} + P_{x_0+2} + P_{x_0+3}} \quad (2)$$

The formulas for 5-COG ($n = 5$) are obtained similarly (not described here). Figure 1d shows the three-point Gaussian (3-Gauss) algorithm that fits the intensity distribution over three pixels to a Gaussian function

$$x_c = x_0 + \frac{\ln(P_{x_0+1}) - \ln(P_{x_0-1})}{2[2\ln(P_{x_0}) - \ln(P_{x_0-1}) - \ln(P_{x_0+1})]} \quad (3)$$

Although this calculation contains a logarithm function, a table of logarithm values can be loaded for reference on FPGA.

In the 2D approach, there are two COG calculations (Figure 1, parts e and f) and two Gaussian fitting methods (Figure 1, parts g and h). The 2D center-of-gravity (2D-COG) expresses x_c as

$$x_c = \frac{\sum_i x_i P_i}{\sum_i P_i} \quad (4)$$

where x_i and P_i denote x and the pixel value, respectively, of the ith pixel member. 2D-COG utilizes the pixel value (Figure 1e). On the other hand, a-COG (Figure 1f) considers only the area of the light spot and discards intensity information

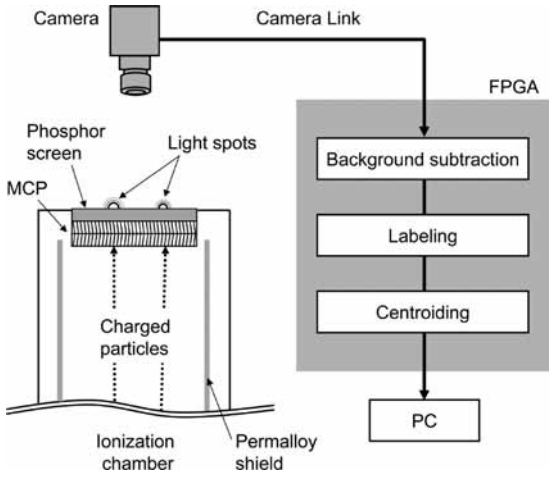

Figure 2. Schematic diagram of the 2D detector and image processing system for real-time high-resolution charged particle imaging. The centroiding calculation code is loaded on the FPGA circuit.

$$x_c = \frac{\sum_i x_i}{n} \quad (5)$$

The two Gaussian fitting methods are referred to as p-Gauss (Figure 1g) and w-Gauss (Figure 1h) on the basis of the following 1D Gaussian fitting. The data set (q_i, P_i), where q_i and P_i denote the pixel position (with a one-unit interval along the q-axis) and its intensity, respectively, is fitted to a Gaussian function by the least-squares method.[19] The center position (g_q) of the fitted Gaussian shape is expressed by

$$g_q = \bar{q} - \frac{(n^2 - 4)[2c_2 - (n + 1)c_1]}{10[6c_3 - 6(n + 1)c_2 + (n + 1)(n + 2)c_1]} \quad (7)$$

where $\bar{q}$ is the average of q_i, n is the number of pixels, and c_n are given as follows

$$c_1 = \sum_{i=1}^{n} \ln(P_i)$$

$$c_2 = \sum_{i=1}^{n} i \ln(P_i)$$

$$c_3 = \sum_{i=1}^{n} i^2 \ln(P_i) \quad (8)$$

The p-Gauss algorithm fits the 1D-projected curves on the $x-z$ and $y-z$ planes to Gaussian functions to calculate x_c and y_c, respectively (Figure 1g). The value of the projection on the $x-z$ plane, P_x', is the sum of the pixel values $P(x,y)$ for all y values in one signal spot

$$P_x' = \sum_y P(x, y) \quad (9)$$

g_x calculated using eq 7 for the set of (x,P_x') is employed as the centroid (x_c) of p-Gauss. The w-Gauss algorithm calculates the Gaussian centers of each column (row) and their weighted mean (Figure 1h). First, the center position for each x, $x_G(x)$, is calculated by fitting the set of $(y, P(x,y))$ to a Gaussian function. Then, the centroid (x_c) is determined by taking their weighted mean as

$$x_c = \sum_x w(x)x_G(x) / \sum_x w(x) \quad (10)$$

where the weight $w(x)$ is the sum of pixel values expressed by

$$w(x) = \sum_y P(x, y) \quad (11)$$

III. FPGA Centroiding System

We have developed our FPGA imaging system in two steps. In the first step, we constructed an imaging system that detects

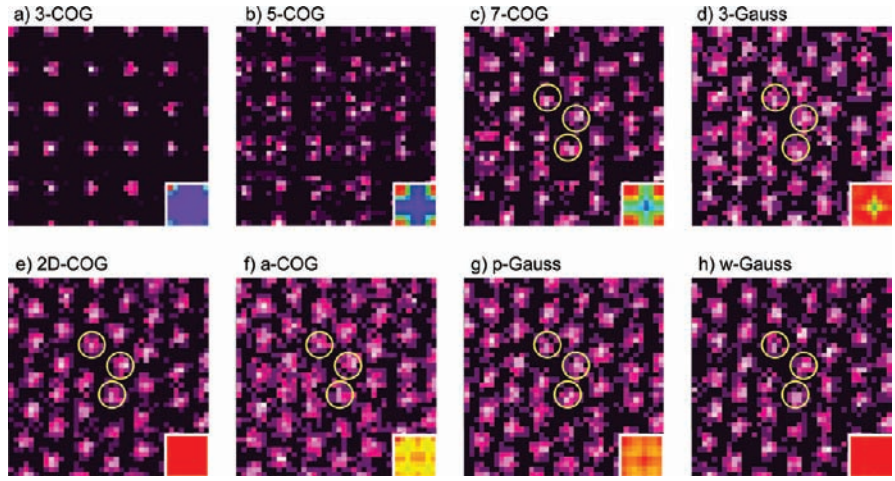

Figure 3. The 8 × 8 subpixel resolution images of the observed MCP pore structure. The area shown is 5 × 5 original pixels (40 × 40 in subpixels). Yellow circles correspond to the diameter of the pore (25 μm). The inset in each figure shows the 8 × 8 super-resolution image corresponding to one camera pixel, averaged over 40000 different camera pixels (expanded ones are shown in Figure 4).

a light spot in the image frame, labels the light spot, and records the selected and labeled portions of an image in the computer memory. After storing these data for a number of image frames, we performed off-line image processing. Since only portions of an image were recorded, the data size was much smaller than those of unprocessed streaming images. In this off-line approach, various centroiding algorithms were easily coded and their performances were compared. In the second stage, we coded the best-performing algorithms in an FPGA circuit and carried out measurements, in which the FPGA circuit executed centroiding and subpixelation in real time. At the same time, we labeled light spots and recorded the related area of an image for off-line analysis. By using this duplicate processing, online processing was double-checked by off-line processing to ascertain performance. After confirming the performance of the FPGA circuit, only online processing was employed in the measurements.

A schematic diagram of our 2D detector and image processing system is shown in Figure 2. This is the system employed in the second stage of our development and is the final form. The detector consists of a Chevron-type (dual) MCP assembly (Burle, 3075FM, 10 μm diameter pore and 12 μm pore-to-pore pitch) backed by a phosphor screen (P20), a CCD camera (Hamamatsu C9300, progressive interline CCD, 2048 × 2048 pixels, 6.5 and 11.5 frames/s with 1 tap and 2 tap readout, respectively), and a personal computer (PC) with an FPGA board. Charged particles (ions or electrons) are generated by laser ionization of a molecular beam in the vacuum chamber. Photoelectrons or photoions are accelerated toward a 2D detector by an electrostatic lens. We used the velocity mapping electrodes similar to the design proposed by Eppink and Parker[20] and modified by Wrede et al.[21] The field-free drift region is shielded by a permalloy tube against a terrestrial magnetic field. An image of the phosphor screen is captured by the camera. Each image frame is transferred through a Camera Link interface to a PC board (Image Technology Laboratory, ITL-PXIO-60L1G2C) equipped with FPGA circuits (Xilinx XC4 VLX60, 26624 slices). The number of light spots in a single frame is limited to 256 in the present real-time image processing system. This maximum number is never too low, because the generation of too many charged particles in a confined space leads to a space charge effect that may distort the velocity distributions of the particles. In our experiments, the number of charged particles detected for a single laser shot was adjusted to be less than 100.

The image data in each camera frame is processed by the following procedure. First, a background image, such as characteristic dark counts of an image sensor, is subtracted from a raw image frame. Then, the labeling logic array circuit searches for the sequence of CCD pixels with a value higher than a certain threshold. If the size of the connecting pixels satisfies a prefixed condition given by an experimenter, the pixels are recognized as a member of the same light spot and labeled with a particular number. Finally, the centroid of each light spot is calculated using a preselected algorithm. The intensity of each light spot is determined to be as unity (event counting), and the calculated centroid (x_c, y_c) with subpixel accuracy is registered. The algorithms (*n*-COG, 3-Gauss, 2D-COG, and a-COG) are loaded on the FPGA circuit for calculation on hardware (hardware centroiding mode) when the imaging program is executed. Other algorithms can also be loaded on the FPGA using HDL. In the off-line mode, the program for centroiding is coded by standard C language as a DLL (dynamic link library). This mode is useful for testing complex algorithms, before their implementation into FPGA circuits.

IV. Results and Discussion

A. Comparison of Centroiding Algorithms. We examined FPN for each centroiding algorithm by observing the pore structures of the MCP assembly. For this performance test, we employed a Z-stack (three-stage) MCP (Hamamatsu F2226-34PGFX) with an MCP pore diameter of 25 μm and a 31 μm pitch. The effective diameter of the MCP was 78 mm. A filament located at 500 mm from the MCP surface was used as an excitation source for the uniform illumination of the MCP. The diameter of a light spot on the phosphor screen was within 6−12 camera pixels. When the camera was set to capture the entire phosphor screen in full frame (2048 × 2048 pixels), a unit pixel corresponded to an area of 38 μm × 38 μm on the screen. Each light spot in an image frame was identified and labeled by real-time processing at a rate of 11.5 frame/s for 12 h.

We employed eight different algorithms for off-line centroiding calculations for comparison. The results obtained from the same original image are shown in Figure 3. The original image has 5 × 5 camera pixels; however 8 × 8 subpixelation made it into a 40 × 40 pixel super-resolution image. After subpixelation, a unit subpixel corresponds to 4.8 μm in real length, which is 1/5 of the diameter of the pore. It is clearly seen that these algorithms produced different images. The inset in each figure

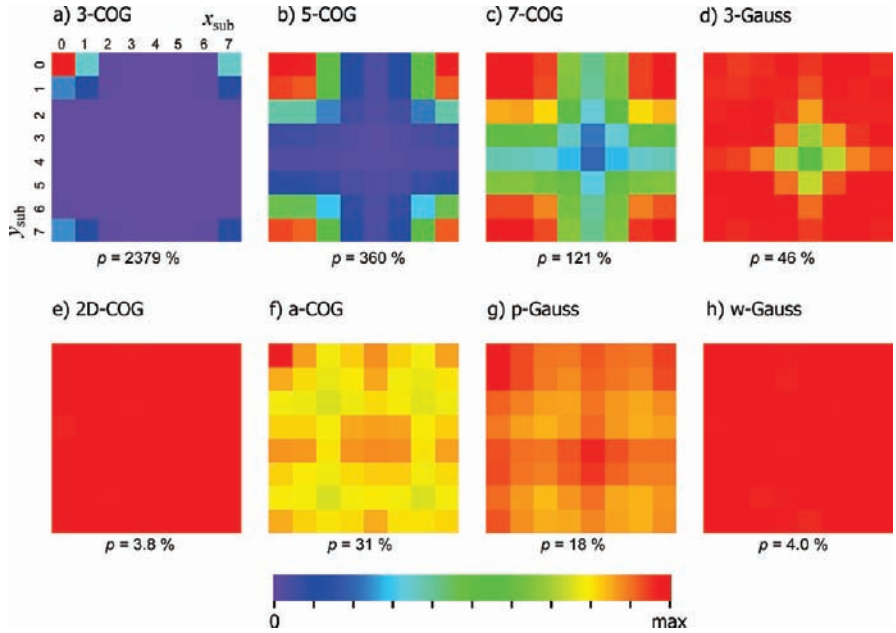

Figure 4. 8 × 8 super-resolution image corresponding to one camera pixel, averaged over 40000 different camera pixels. Fixed pattern noise parameters (p) are also shown.

shows an 8 × 8 image, corresponding to one pixel size of the original camera frame, averaged over the 40000 different camera pixels. Their enlarged views are also presented in Figure 4. If there is no FPN, the average image should appear uniformly, because the pore structure and the arrays of the camera pixels were randomly aligned. However, FPN appears clearly for 3-COG and 5-COG. In particular, the image in Figure 3a represents only FPN and no pore structure. We found that the 3-COG algorithm yielded the centroid mostly at the corners of the average 8 × 8 subpixel unit; i.e., $(x_{sub}, y_{sub}) = (0, 0), (0, 7), (7, 0), (7, 7)$ in Figure 4a. Since the three points (the most intense pixel and its two neighbors) for both the x and y directions are almost equal in intensity for the light spot with the 6−12 pixel diameter, the second term of eq 1 is almost zero and $x_c \approx x_0$ ($y_c \approx y_0$). Thus, the decimal parts of x_c and y_c are nearly zero in 3-COG. This typical FPN is reduced in increasing n-points in n-COG algorithms (5-COG in Figure 4b, 7-COG in Figure 4c).

FPN is often quantified by the FPN parameter (p) defined as follows:[16]

$$p = \frac{\max - \min}{\text{mean}} \times 100(\%) \qquad (12)$$

The p-parameters, which are indicated for each algorithm in Figure 4, were 2379%, 360%, and 121% in 3-COG, 5-COG, and 7-COG, respectively. Michel et al.[16] investigated the effect of the spatial width of the signal on FPN by simulations. For 3-COG and 9-COG, they found that the p-parameter rapidly increases with the width of a signal spot; the p-parameter reaches 100% for a full width at half-maximum (fwhm) of ∼1.4 pixels. For spot images with the fwhm >1 pixel, they showed that Gaussian algorithms (3-Gauss and 9-Gauss) provide much smaller p values than the center-of-gravity algorithms (3-COG, 9-COG). Because pixels further from the most intense pixel have larger weights in the COG algorithms (see eq 2, for example), FPN decreased as the number of sampling points increased to match the spot size. However, such important pixels further from the maximum have lower intensity and are greatly affected by background noise. Additionally, the n-COG algorithms use only two independent 1D (x and y) data arrays, discarding the 2D spread of a light spot. The centroid points obtained from 1D data arrays tend to stay at the corners in an 8 × 8 subpixel unit even for larger n numbers (Figure 4a−c). This was improved by the 3-Gauss algorithm, whose FPN is shown in Figure 4d. Although 3-Gauss uses the same three points as 3-COG, a much smaller p parameter was obtained for 3-Gauss than for any of the n-COG algorithms. Nevertheless, the 3-Gauss algorithm is still based on the 1D fitting of the original 1D data arrays. Therefore, we searched for the further suppression of FPN by fully utilizing the 2D data. This was performed using a p-Gauss algorithm, whose FPN is shown in Figure 4g. The p-Gauss algorithm uses the fitting of two independent 1D data arrays (x and y directions) similarly to the n-COG and 3-Gauss algorithms; however, each 1D data array was a projected distribution of the original 2D data matrix in the x or y direction. No pixel data were discarded in the p-Gauss algorithm. Compared with the 3-Gauss algorithm (Figure 4d), the p-Gauss algorithm (Figure 4g) clearly suppressed the FPN. The suppression was quantified by the p parameters of the p-Gauss (18%) and 3-Gauss (46%).

We have attempted a more effective use of the image data by the 2D-COG, a-COG, and w-Gauss algorithms. All of these algorithms use the entire image data of the light spots. a-COG calculates the center of gravity of the area, and it does not use the intensity distribution but only the positional distribution. The averaged 8 × 8 subpixel unit showed no improvement of FPN in Figure 4f, which had a p parameter of 31%. FPN was markedly improved by the 2D-COG and w-Gauss algorithms. Both algorithms fully used 2D image data, the intensities, and the (x, y) positions. The p parameters were 3.8% and 4.0% for 2D-COG and w-Gauss, respectively, which are comparable with the variation in brightness of light spots on the phosphor screen due to the pulse height distribution of the electron pulse from an MCP. FPN was sufficiently suppressed by these algorithms. The advantage of the Gaussian fitting, which was clearly seen as the difference between 3-COG and 3-Gauss, was not obtained by w-Gauss over 2D-COG. This is because the n-number of 2D-COG was appropriate for the size of the light spot. When

the n-number has to be reduced for some reasons, the w-Gauss algorithm is more effective in suppressing FPN.

We evaluated spatial resolution by observing the pore structure in Figure 3. As described above, the image obtained by 3-COG (Figure 3a) was almost entirely FPN, while 2D-COG and w-Gauss (Figure 3, parts e and h) clearly showed the pore structure with minimal FPN. The images of the pore and FPN are easily distinguished with reference to the average 8 × 8 subpixel unit shown in Figure 4. The pore structure appears more clearly as the p parameter decreases from the 1D algorithms (3-COG, 5-COG, 7 COG, 3-Gauss) and the projected 1D algorithm (p-Gauss) to the 2D algorithms (a-COG, 2D-Gauss, w-Gauss). The yellow circles superimposed in Figure 3c−h represent the 25 μm diameter pore of the MCP. It is seen that the circles match well with the observed image. From the observed minimum structure (pore diameter) and the entire field of view (diameter of phosphor screen, 78 mm), the spatial resolution ($\Delta R/R$) in the present system is evaluated to be higher than 0.03% (=25 μm/78 mm).

B. High-Resolution Photoelectron Imaging for Ionization of NO and Benzene by Real-Time Centroiding. In order to take full advantage of the spatial resolution in charged-particle imaging, the aberration of the electrostatic lens that accelerates charged particles to the MCP detector should be sufficiently small. If the electrostatic lens can focus the trajectories of charged particles within the resolution of the imaging system, the velocity resolution ($\Delta v/v$) of the total charged particle imaging reaches the spatial resolution ($\Delta v/v = 2\Delta R/R$, assuming that the entire scattering distribution fits the detector area and that the origin of the velocity is located in the center of the image).

Prior to the experimental verification of the performance of the detector, we examined electron trajectories in our photoelectron imaging setup by numerical simulations (Simion 3D). Our conclusion is summarized as follows: (i) Electron trajectories can converge to achieve a velocity resolution of 0.1%, if the ionization conditions are ideal. (ii) However, convergence sensitively depends on the position of ionization in the acceleration region, which is usually cylindrical owing to the overlap of a molecular beam and an ionization laser. (iii) Therefore, ultimately high resolution requires an extremely small ionization volume or the design of electrodes that enable the simultaneous convergence of trajectories both parallel and perpendicular to the axis of the cylindrical ionization volume.

We used the conventional design of circular electrodes in the present measurement, as shown in Figure 5a. Voltage was applied independently to the repeller (V_{rep}) and extractor (V_{ext}). The voltages of the other electrodes were passively regulated by the dividing registers in vacuum. This design provided slightly different focusing for the parallel and perpendicular directions of the axis of the ionization volume; therefore, total velocity resolution is limited by the charged particle optics. Nevertheless, the optimal ratio of V_{rep} to V_{ext} was experimentally determined by monitoring the energy resolution in the photoelectron image of NO. The result of the optimization is shown in Figure 5b. The optimal ratio was $V_{ext}/V_{rep} = 0.811$, at which the resolution degraded as a V-shape with respect to V_{ext}/V_{rep}. Optimized energy resolution was very sensitive to V_{ext}/V_{rep} ratio, and accurate power supplies (Matsusada HSX-3R5, ±3.1 kV max., 0.017% accuracy) were used.

The total imaging resolution, which is affected by laser ionization conditions, charged particle optics, and 2D PSD, was evaluated by photoelectron imaging with resonance-enhanced multiphoton ionization photoelectron spectroscopy (REMPI-PES) of NO. In this experiment (and the experiment on benzene described below), Chevron MCP (see section III) is employed. Jet-cooled NO in a molecular beam was ionized by (1 + 1) REMPI via $A^2\Sigma^+ - X^2\Pi$ electronic transition. The output of a YAG-pumped dye laser was frequency-doubled to tune ultraviolet wavelength at 226.249 nm, which induces the ionization via the $N = 0$ rotational level of the $A^2\Sigma^+$ $v = 0$ state. The ionization from this intermediate state dominantly occurs with a selection rule of $\Delta v = 0$ and $\Delta N = 0$, yielding a photoelectron kinetic energy (PKE) of 1.696 eV. The additional sub-bands with $\Delta N = +1$ and $+2$ transitions have intensities less than 10% of that of the main band. The shifts of the PKE are 0.6 meV ($\Delta N = +1$) and 1.5 meV ($\Delta N = +2$). The width of a photon energy was as small as 0.1 cm^{-1} (12 μeV).

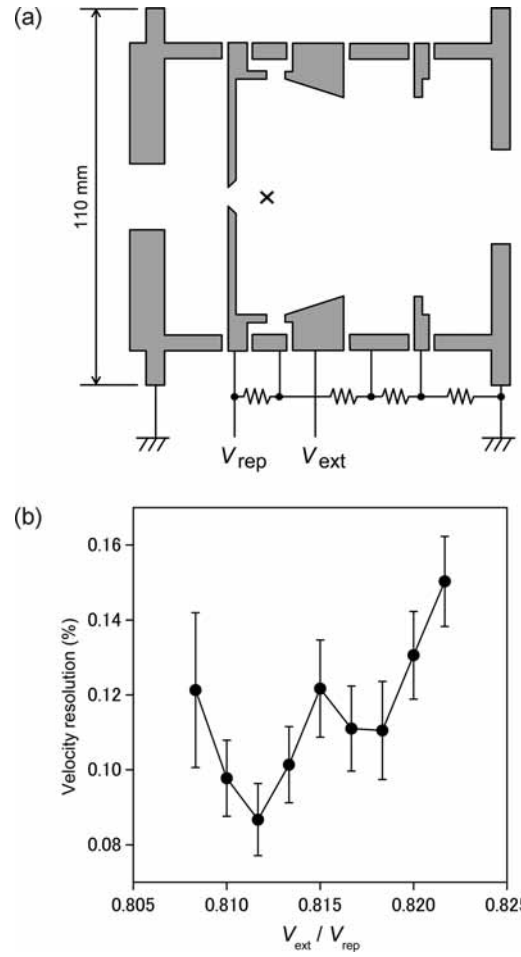

Figure 5. (a) Cross-sectional view of the circular electrostatic lens for the imaging of charged particles. The molecular beam introduced from the left is irradiated by ionization laser light at the position indicated by a cross (×). (b) Velocity resolution in photoelectron imaging of NO as a function of V_{ext}/V_{rep}. V_{rep} was set to −600 V and V_{ext} was varied in 1 V steps (−485 − −493 V). NO is ionized by (1 + 1) REMPI via the $A^2\Sigma^+$ ($v = 0$, $N = 0$) state. Velocity resolution is determined from the fwhm of the Gaussian function fitted to the photoelectron kinetic energy distribution. The error bar is the fitting error of the fwhm.

The observed photoelectron image of NO with real-time centroiding calculation is shown in Figure 6a. This image was obtained for 180000 laser shots (2 h at a repetition rate of 25 Hz). On average, about 90 light spots were detected in each camera frame (6.5 frames/s). Their centroids were calculated using the 2D-COG algorithm in real time, yielding a high-resolution (8192 × 8192 pixels) photoelectron image. Figure 6b presents an expanded view of the rectangular region indicated

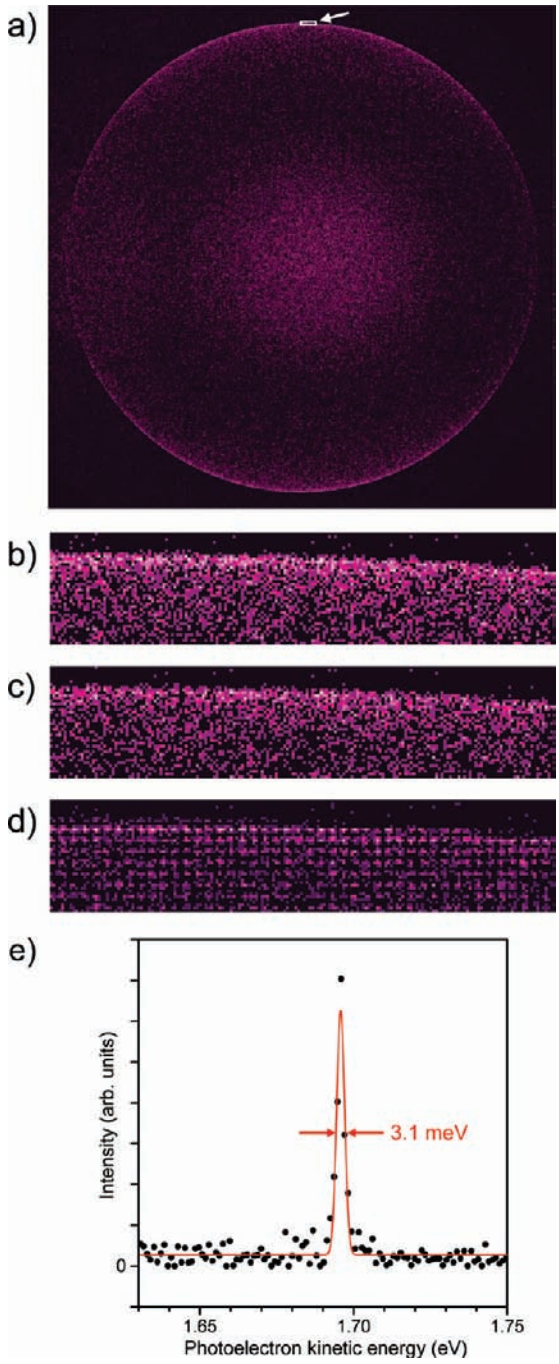

Figure 6. (a) Observed photoelectron image of NO obtained by online centroiding using 2D-COG algorithm. The 6100 × 6100 region selected from the recorded 8192 × 8192 pixels is displayed. Laser polarization is in the vertical direction in the figure. NO is ionized by (1 + 1) REMPI via the $A^2\Sigma^+$ ($v = 0$, $N = 0$) state under the electrode condition of $V_{rep} = -600$ V, $V_{ext} = -487$ V. (b−d) Expanded views of the indicated region in (a). Subpixelation was executed by (b) 2D-COG (real-time), (c) w-Gauss (off-line), and (d) 3-COG (off-line) for the same image. (e) Photoelectron kinetic energy distribution obtained from the image (a). Each dot is from pBASEX fitting. The solid red line is the fitted Gaussian, showing an fwhm of 3.1 meV. Energy resolution is calculated to be 0.2%.

in Figure 6a. For comparison, the off-line centroiding results with the w-Gauss and 3-COG algorithms for the same image are displayed in parts c and d of Figure 6, respectively. The ring structure is clearly seen in both parts b and c of Figure 6, demonstrating the good performance of 2D-COG and w-Gauss for this observation. However, the image obtained by 3-COG clearly shows FPN (Figure 6d).

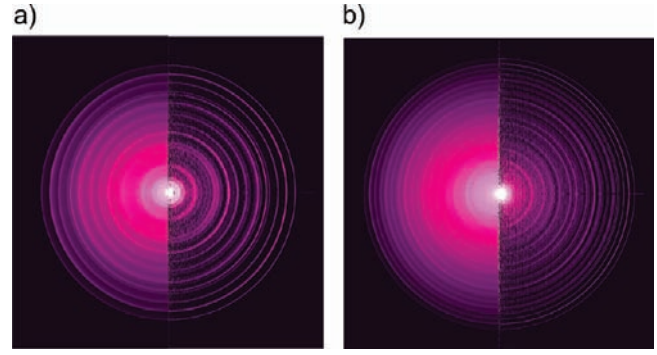

Figure 7. Photoelectron images of the benzene molecules ionized by (1 + 1) REMPI using the $S_1 \leftarrow S_0$ vibronic band of (a) 6_0^1 at 259.0 nm and (b) $1_0^1 6_0^1$ at 252.9 nm: left half, observed image; right half, slice image obtained by inverse Abel transform. Laser polarization is vertical in the figure. A number of the concentric rings correspond to the quantized vibrational levels in the ground electronic state of the benzene cation.

The observed image shown in Figure 6a was analyzed to extract the slice image by the polar basis set expansion (pBASEX) method.[22] The obtained PKE distribution by integrating over the whole scattering angle ($0 - \pi$) is shown in Figure 6e. The width of the peak was 3.1 meV (fwhm). This width results from the final state distribution of NO^+ (<1.5 meV), the energy width of the light source (12 μeV), the resolution of the 2D detector (<2.0 meV), and the aberration of ion optics (>3 meV). The result clearly shows that a total energy resolution of $\Delta E/E = 0.2\%$ was achieved. With this resolution, it should be possible to carry out state-to-state photoionization of small molecules such as NO without using a time-of-flight detector and observing the entire angular distribution simultaneously. High-resolution 2D PSD is useful for detailed studies of the photoionization dynamics of molecules.

It is also interesting to apply this apparatus to observation of vibrationally resolved photoelectron images for large polyatomic molecules. Thus, we carried out the photoelectron imaging of benzene in a supersonic molecular beam by one-color (1 + 1) REMPI using the $S_1 - S_0$ transitions of 6_0^1 at 259.0 nm and $1_0^1 6_0^1$ at 252.9 nm. As shown in Figure 7, the photoelectron images with 2048 × 2048 pixel resolution consist of sharp rings due to vibrational energy levels in the ground state of the cation. More precisely, the ground state of the cation ($^2E_{1g}$) is doubly degenerate, and ionization occurs to the two Jahn−Teller components with vibronic angular momenta of $j = 1/2$ and 3/2. The observed images (left-hand sides of parts a and b of Figure 7) were transformed into 2D slice (right-hand sides) through 3D distribution by the inverse Abel transform. The photoelectron angular distributions exhibit a slight preference for photoemission perpendicular to laser polarization. Spectra a and b of Figure 8 show the photoelectron kinetic energy spectra (plotted as a function of ion internal energy) obtained by integrating the angular parts of the slice images for REMPI via 6^1 and $1^1 6^1$, respectively. The photoelectron spectra agreed quite well with those in the previous report by Long et al. using a time-of-flight method[23] except that the TOF method was unable to detect low-energy electrons. Table 1 lists the observed peak positions and the vibronic assignments made by referring to MATI (mass-analyzed threshold ionization spectroscopy).[24] The energy width of the observed vibronic bands was about 6 meV, comparable to that obtained by the TOF method.[23] The bandwidth rather broader than the expected performance of the imaging system is partly attributed to the high rotational temperature of benzene in our molecular beam in the present experiment. The lower

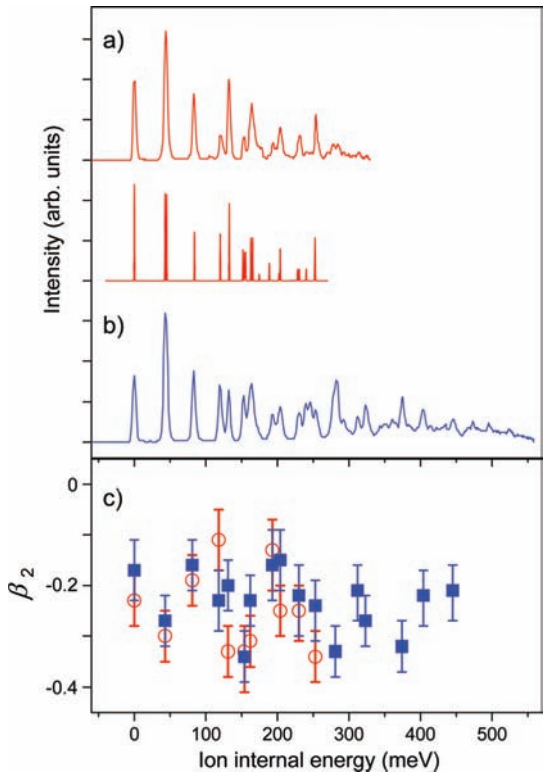

Figure 8. (a, b) Photoelectron spectra obtained from the photoelectron images of benzene (Figure 7) plotted against ion internal energy. The $S_1 \leftarrow S_0$ transitions used for the measurement were (a) 6_0^1 and (b) $1_0^1 6_0^1$. The lower trace in (a) is the simulated spectrum using the peak positions and intensities in ref 24 convoluted with the Gaussian line-shape function of fwhm = 0.7 meV (energy resolution of 0.2% at the outermost ring). (c) β_2 parameters observed for each vibronic peak. Open red circles and closed squares represent the values obtained with the excitation transitions of 6_0^1 and $1_0^1 6_0^1$, respectively.

TABLE 1: Observed Peak Positions and Anisotropy Parameters[a,b]

	PKE (meV)		β_2		β_4	
assignments	6_0^1	$6_0^1\,1_0^1$	6_0^1	$6_0^1\,1_0^1$	6_0^1	$6_0^1\,1_0^1$
origin	329	558	−0.23	−0.17	−0.02	−0.03
6^1(3/2)	285	515	−0.30	−0.27	0.00	−0.03
6^1(1/2)	246	475	−0.19	−0.16	0.03	0.00
1^1	208	438	−0.11	−0.23	0.03	−0.01
6^2(1/2)	196	426	−0.33	−0.20	0.00	−0.05
6^3(3/2)	176	405	−0.33	−0.34	0.09	0.05
$1^1 6^1$(3/2)	165	394	−0.31	−0.23	0.02	−0.04
8^1(1/2)	136	365	−0.13	−0.16	0.13	0.04
6^2(3/2)	125	355	−0.25	−0.15	0.04	−0.03
$6^2 9^1$(3/2)	98	328	−0.25	−0.22	0.07	0.06
6^4(1/2)	75	305	−0.34	−0.24	0.02	−0.01
		276		−0.33		0.01
		245		−0.21		0.07
		235		−0.27		0.02
		183		−0.32		0.04
		155		−0.22		0.03
		112		−0.21		0.04

[a] β_2 and β_4 are the averages of the four quadrants of an observed image. The accuracies are estimated to be less than ±0.05 for most of the bands. See Figures 8c and 9 for individual error ranges. [b] Assignments were made in accordance with ref 24.

trace of Figure 8a is the simulated spectrum with the Gaussian line shape function of fwhm = 0.66 meV (energy resolution of 0.2% at the outermost ring), in which the peak positions and intensities tabulated in ref 24 were used. Further optimization

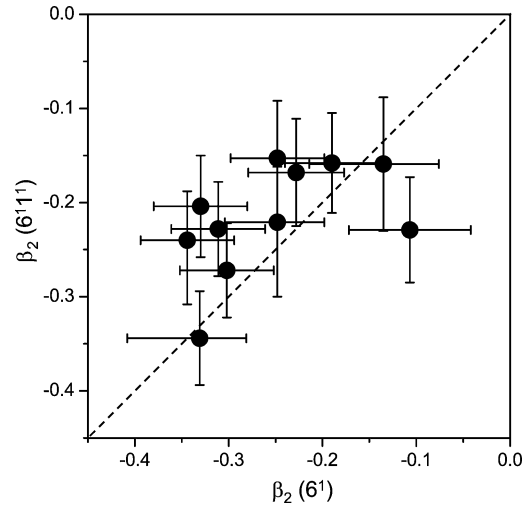

Figure 9. Correlation between $\beta_2(6^1)$ (β_2 measured with 6_0^1 transition) and $\beta_2(6^1 1^1)$ (with $1_0^1 6_0^1$ transition) for the same final vibronic states in the cation. The broken line correspond to $\beta_2(6^1) = \beta_2(6^1 1^1)$.

of our apparatus to observe such an ultimate resolution for benzene is in progress.

Another advantage of photoelectron imaging is the capability of measuring the photoelectron angular distribution associated with each vibronic transition. We analyzed the observed angular distribution [$I(\theta)$] using a standard formula for two-photon ionization:

$$I(\theta) = 1 + \beta_2 P_2(\theta) + \beta_4 P_4(\theta) \qquad (13)$$

where θ is the angle between the **k** vector of the electron and the laser polarization direction in the laboratory frame, and P_2 and P_4 are the second- and fourth-order Legendre polynomials. The anisotropy parameters (β_2 and β_4) determined for each band are listed in Table 1, and the β_2 values are also plotted in Figure 8c. These anisotropy parameters were the average values obtained by independent analyses of the four quadrants of the same image. In order to confirm the analysis using inverse Abel transform, we also carried out inverse Abel transform of the image fitted by pBASEX to the observed 2D projection (pBASEX fitting has smoothed the raw image). When pBASEX was used, the anisotropy parameters appeared slightly lower than those obtained by direct inverse Abel transform of the raw image. The estimated errors in anisotropy parameters were generally less than ±0.05, while we estimated slightly larger errors for some of the bands that exhibited lower anisotropy parameters in the analysis using pBASEX. These errors are presented as bars associated with the data points in Figures 8c and 9. The β_2 values are in the range between −0.1 and −0.4 and the β_4 values are almost zero.

The photoelectron angular distribution is determined by a photoelectron scattering wave that varies with the photoelectron kinetic energy and the vibronic state of the cation produced by ionization. Figure 8c plots β_2 as a function of ion internal energy to examine the vibronic state dependence. As an example, β_2 observed for 6^1(3/2) is lower than those for 0^0 and 6^1(1/2), clearly indicating the vibronic state dependence. The correlation between $\beta_2(6^1)$ (β_2 measured with 6_0^1 transition) and $\beta_2(6^1 1^1)$ (with $1_0^1 6_0^1$ transition) is examined in Figure 9. If $\beta_2(6^1)$ and $\beta_2(6^1 1^1)$ are the same, the data point should be on the diagonal broken line. Although the points are not on any straight line, there is a clear positive correlation between $\beta_2(6^1)$ and $\beta_2(6^1 1^1)$.

Also noticed in Figure 9 is that most of the points appear above the diagonal line, indicating that $\beta_2(6^1 1^1)$ is larger than $\beta_2(6^1)$. This is attributed to the increase of photoelectron kinetic energy by 330 meV in the former than the latter: even if the composition of the electron scattering partial waves is the same, the change of kinetic energy leads to variation of Coulomb phases of the partial waves and affects photoelectron angular anisotropies.

Summary

Resolution enhancement in photoelectron imaging was achieved up to $\Delta E/E = 0.2\%$ by real-time subpixel centroiding calculations implemented with a field-programmable gate array circuit. The performances of the eight different algorithms of centroiding were examined by observing the pore structure of an MCP. Among the one-dimensional algorithms (3-COG, 5-COG, 7-COG, 3-Gauss), the projected one-dimensional algorithm (p-Gauss) and the two-dimensional algorithms (a-COG, 2D-COG, w-Gauss), 2D-COG and w-Gauss, provided the best result with minimal fixed pattern noise. The spatial resolution ($\Delta R/R$) of the imaging system was evaluated to be better than 0.03%. The entire system of photoelectron imaging was examined by observing the photoionization of NO via the A state by (1 + 1) REMPI spectroscopy. The obtained PKE resolution ($\Delta E/E$) of 0.2% is currently limited by the aberration effects of charged particle optics employed in the present work and can be improved in the future. However, the current resolution is already sufficiently high to carry out a rotationally resolved photoionization study of small molecules. The method was also applied to the (1 + 1) REMPI of benzene with 6_0^1 and $1_0^1 6_0^1$ transitions, and the PKE spectra and photoelectron angular anisotropy were obtained. Variation in the anisotropy parameter for the photoelectron kinetic energy and the vibronic state of the cation were observed.

Acknowledgment. This study was supported in part by the X-ray Free Electron Laser Utilization Research Project of the Ministry of Education, Culture, Sports, Science and Technology of Japan (MEXT). Y.O. acknowledges the Special Postdoctoral Researcher Program at RIKEN. T.S. thanks Professor Idaku Ishii at Hiroshima University for valuable advice in the early stage of this work.

References and Notes

(1) Kawamata, H.; Kohguchi, H.; Nishide, T.; Suzuki, T. *J. Chem. Phys.* **2006**, *125*, 133312.

(2) Lipciuc, M. L.; Buijs, J. B.; Janssen, M. H. M. *Phys. Chem. Chem. Phys.* **2006**, *8*, 219.

(3) Cavanagh, S. J.; Gibson, S. T.; Gale, M. N.; Dedman, C. J.; Roberts, E. H.; Lewis, B. R. *Phys. Rev. A* **2007**, *76*, 052708.

(4) Horio, T.; Suzuki, T. *Rev. Sci. Instrum.* **2009**, *80*, 013706.

(5) Landi, G. *Nucl. Instrum. Methods Phys. Res., Sect. A* **2003**, *497*, 511.

(6) Tremsin, A. S.; Vallerga, J. V.; Siegmund, O. H. W. *Nucl. Instrum. Methods Phys. Res., Sect. A* **2002**, *477*, 262.

(7) Landi, G. *Nucl. Instrum. Methods Phys. Res., Sect. A* **2002**, *485*, 698.

(8) Suhling, K.; Airey, R. W.; Morgan, B. L. *Rev. Sci. Instrum.* **2002**, *73*, 2917.

(9) Suhling, K.; Airey, R. W.; Morgan, B. L. *Nucl. Instrum. Methods Phys. Res., Sect. A* **1999**, *437*, 393.

(10) Lau, K.; Pyrlik, J. *Nucl. Instrum. Methods Phys. Res., Sect. A* **1995**, *366*, 298.

(11) Kawakami, H.; Bone, D.; Fordham, J.; Michel, R. *Nucl. Instrum. Methods Phys. Res., Sect. A* **1994**, *348*, 707.

(12) Carter, M. K.; Patchett, B. E.; Read, P. D.; Waltham, N.; van Breda, I. G. *Nucl. Instrum. Methods Phys. Res., Sect. A* **1991**, *310*, 305.

(13) Lapington, J. S.; Kessel, R.; Walton, D. M. *Nucl. Instrum. Methods Phys. Res., Sect. A* **1988**, *273*, 663.

(14) Tremsin, A. S.; Vallerga, J. V.; Siegmund, O. H. W.; Hull, J. S. *Proc. SPIE* **2003**, *5164*, 113.

(15) Vallerga, J. V.; Siegmund, O. H. W.; Dalcomo, J.; Jelinsky, P. N. *Proc. SPIE* **1997**, *3019*, 156.

(16) Michel, R.; Fordham, J.; Kawakami, H. *Mon. Not. R. Astron. Soc.* **1997**, *292*, 611.

(17) Chang, B.-Y.; Hoetzlein, R. C.; Mueller, J. A.; Geiser, J. D.; Houston, P. L. *Rev. Sci. Instrum.* **1998**, *69*, 1665.

(18) Li, W.; Chambreau, S. D.; Lahankar, S. A.; Suits, A. G. *Rev. Sci. Instrum.* **2005**, *76*, 063106.

(19) Kurita, M. *Trans. Jpn. Soc. Mech. Eng., A* **1988**, *54*, 2176.

(20) Eppink, A. T. J. B.; Parker, D. H. *Rev. Sci. Instrum.* **1997**, *68*, 3477.

(21) Wrede, E.; Laubach, S.; Schulenburg, S.; Brown, A.; Wouters, E. R.; Orr-Ewing, A. J.; Ashfold, M. N. R. *J. Chem. Phys.* **2001**, *114*, 2629.

(22) Garcia, G. A.; Nahon, L.; Powis, I. *Rev. Sci. Instrum.* **2004**, *75*, 4989.

(23) Long, S. R.; Meek, J. T.; Reilly, J. P. *J. Chem. Phys.* **1983**, *79*, 3206.

(24) Burrill, A. B.; Chung, Y. K.; Mann, H. A.; Johnson, P. M. *J. Chem. Phys.* **2004**, *120*, 8587.

JP9039995